Effect of Dendritic Arm Spacing on Mechanical Properties and Corrosion Resistance of Al 9 Wt Pct Si and Zn 27 Wt Pct Al Alloys

WISLEI R. OSÓRIO, PEDRO R. GOULART, GIVANILDO A. SANTOS, CARLOS MOURA NETO, and AMAURI GARCIA

It has been reported that the mechanical properties and the corrosion resistance (CR) of metallic alloys depend strongly on the solidification microstructural arrangement. The correlation of corrosion behavior and mechanical properties with microstructure parameters can be very useful for planning solidification conditions in order to achieve a desired level of final properties. The aim of the present work is to investigate the influence of heat-transfer solidification variables on the microstructural array of both Al 9 wt pct Si and Zn 27 wt pct Al alloy castings and to develop correlations between the as-cast dendritic microstructure, CR, and tensile mechanical properties. Experimental results include transient metal/mold heat-transfer coefficient (h_i), secondary dendrite arm spacing (λ_2), corrosion potential (E_{Corr}), corrosion rate (i_{Corr}), polarization resistance (R_1), capacitances values (Z_{CPE}), ultimate tensile strength (UTS, σ_U), yield strength (YS, σ_y), and elongation. It is shown that σ_U decreases with increasing λ_2 while the CR increases with increasing λ_2, for both alloys experimentally examined. A combined plot of CR and σ_U as a function of λ_2 is proposed as a way to determine an optimum range of secondary dendrite arm spacing that provides good balance between both properties.

I. INTRODUCTION

ALUMINUM alloys with silicon as a major alloying element constitute a class of material that provides the most significant part of all shaped castings manufactured, especially in the aerospace and automotive industries.[1] This is mainly due to the outstanding effect of silicon in the improvement of casting characteristics, combined with other physical properties such as mechanical properties and corrosion resistance (CR). In general, an optimum range of silicon content can be assigned to casting processes. For slow cooling rate processes (sand, plaster, and investment), the range is 5 to 7 wt pct, for permanent molds 7 to 9 pct, and for die castings 8 to 12 pct.[2]

Zn-Al alloys (ZA) usually deliver high strength and superior hardness when compared to the aforementioned Al-Si alloys, combined with a good CR. Three members of this family of alloys are generally identified industry-wide as ZA-8, ZA-12, and ZA-27. The numerical components of the alloy designation indicate the approximate aluminum content.[3,4] These alloys were originally intended for gravity casting, but it was found that ZA-12 and ZA-27 could be pressure die cast by the cold-chamber route with impressive results, especially ZA-27, which achieved high values of tensile strength.[5]

The effect of microstructure on metallic alloys properties has been highlighted in various studies and, particularly, the influence of dendrite arm spacing upon the mechanical properties, *i.e.*, ultimate tensile strength (UTS) and yield strength (YS), has been reported.[6–13] Recently, some studies have also focused on dendritic network and corrosion behavior relationships.[14,15,16] Although the metallurgical and micromechanical aspects of the factors controlling microstructure, unsoundness, strength and ductility, and CR of as-cast alloys are complex, it is well known that solidification processing variables are of a high order of importance. In the as-cast state, an alloy may possess within individual grains a dendritic network of continuously varying solute content, second phases, and possibly porosity and inclusions.[9] It is generally found that the grain size reduction increases the metal tensile strength. The well-known Hall–Petch equation shows that the yield strength is proportional to the reciprocal of the square root of the grain diameter.[6,7]

For cast metals, however, it is not always true that the tensile strength improves with decreasing grain size. Strength will increase with grain size reduction only if the production of small grains does not increase the amount of microporosity, the percentage volume of second phase, or the dendrite spacing.[11] Also, it is not always true that a finer structure provides an improvement in the CR. Reports can be found in the literature relating microstructural characteristics with the CR.[14–19] On the other hand, for pure metals castings, the tendency of CR can be connected only with the macrostructural form and grain size due to the absence of representative dendrite branch formation.[11,20,21]

The cooling rate during solidification defines the dendritic network fineness. The solute redistribution, the anodic or cathodic electrochemical behavior of each component of the alloy, and the dendrite fineness are the three main factors affecting the CR of castings.[14,15] It is well known that there is a close correlation between thermal variables and the solidification structure, and as a direct consequence, morphological structure parameters such as grain size and dendritic arm spacing also depend on heat-transfer

WISLEI R. OSORIO, Postdoctoral Fellow, PEDRO R. GOULART, Doctoral Student, and AMAURI GARCIA, Professor, are with the Department of Materials Engineering, State University of Campinas, UNICAMP, 13083 – 970 Campinas, SP, Brazil. Contact e-mail: amaurig@fem.unicamp.br. GIVANILDO A. SANTOS, Doctoral Student, and CARLOS MOURA NETO, Professor, are with the Mechanics and Aeronautics Engineering Division, Aeronautical Institute of Technology, CTA, 12228- 900 São José dos Campos, SP, Brazil.

Manuscript submitted February 14, 2006.

conditions imposed by the metal/mold system. Thus, the control of solidification thermal variables such as tip growth rate (V_L), thermal gradient (G_L), cooling rate ($\dot{T}$), and local solidification time (t_{SL}) permits a range of microstructures to be obtained.[12,13,22,23]

The present work focuses on the influence of heat-transfer transient solidification variables on the microstructural formation of both Al 9 wt pct Si and Zn 27 wt pct Al alloys castings and on the development of correlations between dendritic array spacing, CR, and tensile mechanical properties. The purpose of this article is to provide a method to use solidification parameters to optimize both mechanical and corrosion properties in real applications. Experimental results include the transient metal/mold heat-transfer coefficient (h_i), secondary dendrite arm spacing (λ_2), corrosion potential (E_{Corr}), corrosion rate (i_{Corr}), polarization resistance (R_1), capacitance values (Z_{CPE}), UTS (σ_u), YS (σ_y), and elongation.

II. SOLIDIFICATION THERMAL VARIABLES

Heat flow across the metal casting/mold interface can be characterized by a macroscopic average metal/mold interfacial heat-transfer coefficient, h_i (W m^{-2} K^{-1}), given by

$$h_i = \frac{q}{A(T_{IC} - T_{IM})} \quad [1]$$

where q (W) is the average heat flux, A (m^2) is the area, and T_{IC} and T_{IM} are metal and mold surface temperatures (K) at the interface. It is well known that during the solidification process, the mold gradually expands due to heat absorption, and the metal casting is subjected to shrinkage. As a result, a gap develops due to insufficient contact between the metal and mold, and as a direct consequence, h_i decreases rapidly. In previous articles, the transient interfacial heat-transfer coefficient has been successfully characterized by using an approach based on measured temperatures along the casting and numerical simulations provided by heat-transfer solidification models.[11,16,24–26] This coefficient has been expressed as a power function of time, given by

$$h_i = C_i(t)^{-a} \quad [2]$$

where t (s) is the time from the beginning of cooling during the solidification process, and C_i and a are constants that depend on alloy composition, chill material, and melt superheat.

Solidification thermal variables can be analytically described as a function of metal/mold parameters and casting operational conditions and, consequently, as a function of the metal/mold interfacial heat-transfer coefficient (h_i).[13,23–26] An analytical heat-transfer model describing temperature distribution in liquid, mushy zone, solid, and mold, and the displacement of solidus and liquidus isotherms during the unidirectional solidification of binary alloys, can be used for determining the tip cooling rate.[26] The model has been validated in previous articles[11–13,23,25,26] against experimental results concerning the solidification of Al-Cu, Zn-Al, and Sn-Pb alloys. Equation [3] gives a typical example of the tip cooling rate ($\dot{T}_L$), as a function of h_i. However, other thermal variables such as temperature gradient (G_L), tip growth rate (V_L), and local solidification time (t_{SL}) may also be given as a function of metal/mold solidification parameters, as described in previous articles.[11,13,23–26]

$$\dot{T}_L = \left[\frac{m\,(T_p - T_{\text{Liq}})}{\sqrt{\pi}\cdot\alpha_{SL}\,\phi_2[1-\text{erf}\,(m\phi_2)]\,\exp\,(m\phi_2)^2}\right] \left[\frac{\dfrac{2\alpha_{SL}\phi_2^2}{2K_S\phi_2(T_{\text{Sol}}-T_0)}}{n\sqrt{\pi}(T_{\text{Liq}}-T_0)\,\exp\,(\phi_1^2)[M+\text{erf}(\phi_1)]h_i} + S_L\right]^2 \quad [3]$$

where α_{SL} is the thermal diffusivity of the mushy zone; ϕ_1 and ϕ_2 are solidification constants associated with the displacement of solidus and liquidus isotherms, respectively; K_S is the solid thermal conductivity; T_{Sol} is the nonequilibrium solidus temperature; T_0 is the environment temperature; T_{Liq} is the liquidus temperature; T_p is the initial melt temperature, m is the square root of the ratio of thermal diffusivities of mushy zone and liquid, $(\alpha_{SL}/\alpha_L)^{1/2}$, M is the ratio of heat diffusivities of solid and mold material, $(k_S c_M \rho_M / k_M c_S \rho_S)^{1/2}$, n is the square root of the ratio of thermal diffusivities of solid metal and mushy zone, $(\alpha_S/\alpha_{SL})^{1/2}$, and S_L is the position of liquidus isotherm from the metal/mold interface.

III. EXPERIMENTAL

Figure 1(a) shows the casting assembly used in solidification experiments. The main design criterion was to ensure a dominant horizontal and unidirectional heat flow during solidification. This objective was achieved by adequate insulation of the chill casting chamber. A low carbon steel chill was used at a normal environment temperature of about 25 °C (initial mold temperature), with the heat-extracting surface being polished.

Experiments were performed with Al 9 wt pct Si and Zn 27 wt pct Al alloys, which were melted in an electric resistance-type furnace, degassed in order to minimize porosity incidence, and then poured into the casting chamber with a melt temperature, T_p, of about 10 pct above the liquidus temperature (T_p = 665 °C and 550 °C for Al 9 wt pct Si and Zn 27 wt pct Al, respectively). These alloys were prepared by using commercially pure metals, as described in Table I.

Temperatures in both metal and mold were monitored during solidification using a bank of type J (mold) and K (metal) thermocouples accurately located in the mold (at 3 mm from the casting surface) and along the casting length at six different positions with respect to the metal/mold interface, 3, 13, 23, 33, 43, and 53 mm, at the center of the casting, as indicated in Figure 1(a).

All of the thermocouples were connected by coaxial cables to a data logger interfaced with a computer, and the temperature data were acquired automatically. The thermophysical properties of Al 9 wt pct Si and Zn 27 wt pct Al alloys and the chill material, which were used to run the necessary simulations, are summarized in Table II.

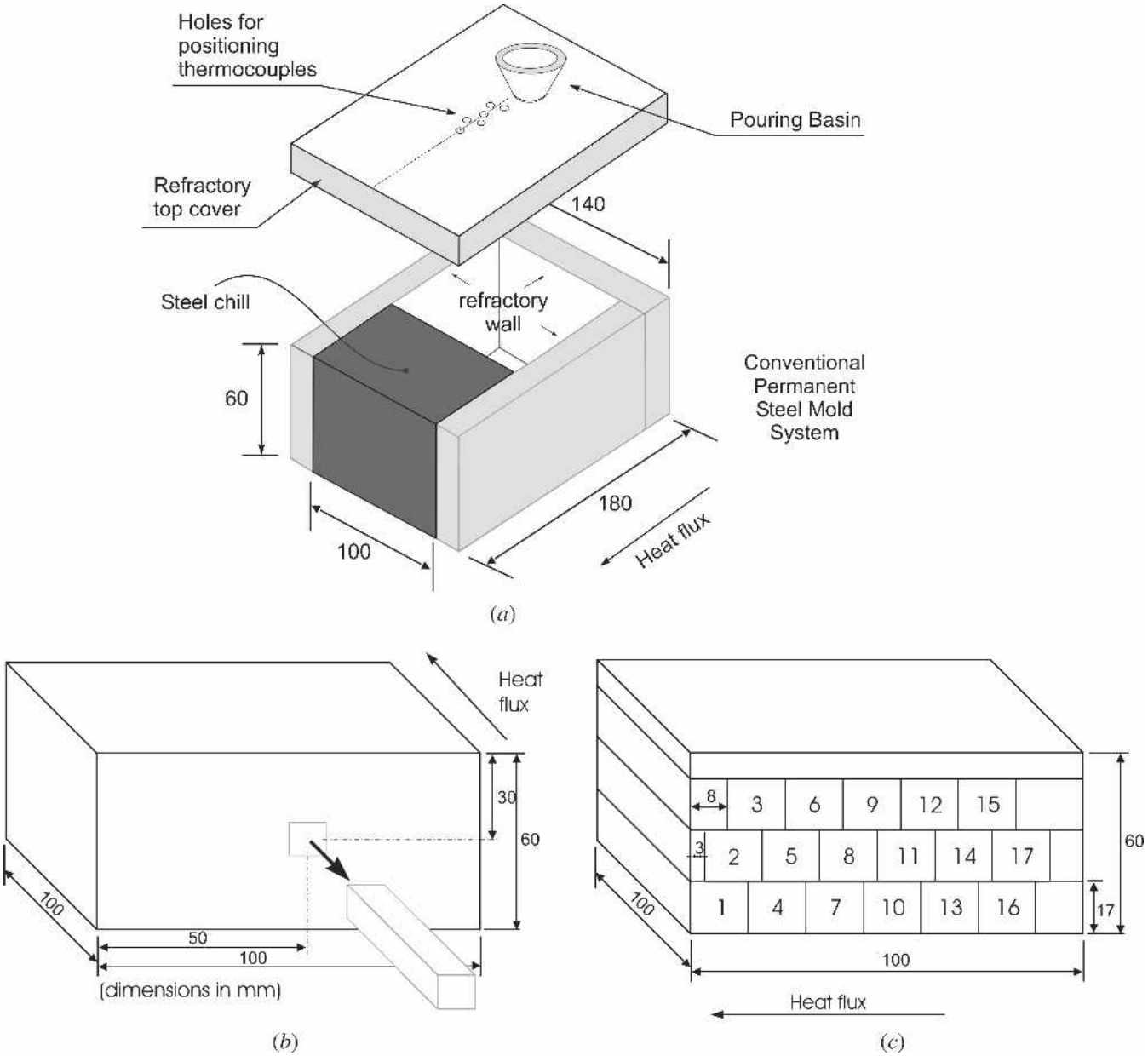

Fig. 1—(*a*) Schematic representation of the casting assembly and location of specimens for (*b*) metallographic procedures and (*c*) tensile testing.

Figures 1(b) and (c) exhibit both the longitudinal and the transversal specimens that were taken for optical metallographic examination and tensile testing according to specifications of ASTM Standard E 8M, respectively. In order to ensure reproducibility of the tensile results, three specimens were tested for each selected position, as indicated in Figure 1(c), and both YS and UTS have been determined at different positions with respect to the chill/casting interface. Longitudinal specimens had selected sections polished and etched for macrostructural and microstructural examination. For the Al-Si alloy, the used etchant was a solution of 0.5 pct HF. The etchant used to reveal the microstructure of the Zn-Al alloy was a solution containing 5 g CrO_3, 0.5 g Na_2SO_4, and 100 mL H_2O and rinsed in a solution of 20 g CrO_3 and 100 mL H_2O.[29]An image processing system was then used to measure the sec-

Table I. Chemical Compositions of Zn, Al, and Si Used to Prepare the Alloys

Chemical Composition of Zn					
Element	Zn	Fe	Pb	Si	Other
(wt pct)	99.97	0.015	0.012	0.003	<0.001
Chemical Composition of Al					
Element	Al	Fe	Pb	Si	Other
(wt pct)	99.93	0.038	<0.001	0.033	<0.001
Chemical Composition of Si					
Element	Si	Fe	Pb	Al	Other
(wt pct)	99.57	0.316	<0.001	0.109	<0.001

Table II. Casting and Chill Materials Used for Experimentation and the Corresponding Thermophysical Properties[8,27,28]

Properties	Symbol/Units	Al 9 Wt Pct Si	Zn 27 Wt Pct Al	Steel SAE 1010
Thermal conductivity (solid)	K_s (W · m^{-1} K^{-1})	81	161	46
Thermal conductivity (liquid)*	K_{Liq} (W · m^{-1} K^{-1})	88.0	73	—
Density (solid)	ρ_s (kg · m^{-3})	2670	5000	7860
Density (liquid)*	ρ_{Liq} (kg · m^{-3})	2399	4800	—
Specific heat (solid)	c_s (J · kg^{-1} K^{-1})	963	749	527
Specific heat (liquid)*	c_{Liq} (J · kg^{-1} K^{-1})	1078	773	—
Latent heat of fusion	L (J · kg^{-1})	405,548	216,950	—
Liquidus temperature	T_{Liq} (°C)	604	500	—
Nonequilibrium solidus temperature	T_{Sol} (°C)	577	382	—
Solute diffusivity	D (mm^2 · s^{-1})	3.10	5.10	—
Partition coefficient	k_0	0.13	3.44	—
Gibbs–Thomson coefficient	Γ (K mm)	9.10	11.10	—
Liquidus slope	m (K/wt pct)	6.0	4.3	—

*The thermophysical properties in liquid state are values corresponding to the liquid temperature close to the liquidus temperature.

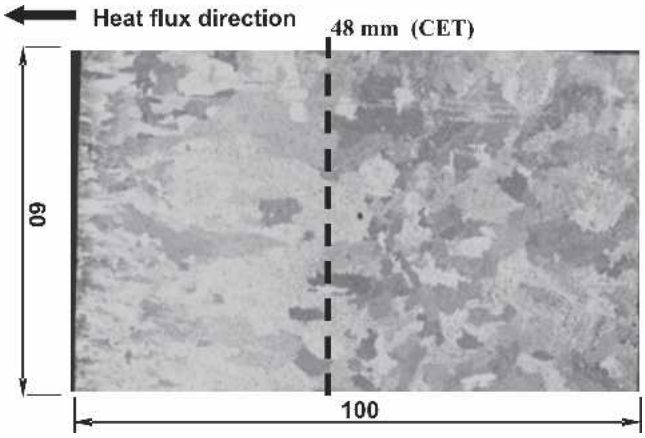

Fig. 2—Typical macrostructural morphology for an Al 9 wt pct Si alloy casting.

ondary dendrite arm spacing for each selected position from the casting surface (20 measurements for each position).

Figure 2 exhibits a typical macrostructure of an Al 9 wt pct Si ingot with the columnar-to-equiaxed (CET) transition occurring at about half of the ingot length (at about 48 mm from the chill/casting surface). Recent studies have shown that the CET depends on critical values of thermal solidification variables and that the solute content in hypoeutectic Al-Si alloys is not found to significantly affect the experimental position of the CET.[27,30] Some investigations on vertically upward solidification of Al-Cu[22] and Sn-Pb[31] alloys have proposed a CET criterion based on critical cooling rates of about 0.2 and 0.014 K/s, respectively, with the columnar growth prevailing throughout the casting for cooling rates higher than these critical values. Peres *et al.*[27] have shown that for hypoeutectic Al-Si alloys, the cooling rate at the CET was about 0.17 K/s, which is quite close to the critical value found for Al-Cu alloys. In the present experimental investigation, a value of about 0.20 K/s has been determined at the CET position. There is no information available in the literature concerning the CET occurrence for a Zn 27 wt pct Al alloy. In the present investigation with this alloy, the CET was characterized by a position at about 50 mm from the metal/chill surface and a cooling rate of about 0.40 K/s.

In order to determine correlations between the CR and the microstructural pattern, electrochemical impedance spectroscopy (EIS) and polarization tests were conducted in a 500 mL volume of a 3 pct NaCl solution at room temperature (25 °C), using a potentiostat coupled to a frequency analyzer system, a glass corrosion cell kit with a platinum counter electrode, and a saturated calomel reference electrode (SCE), as prescribed by the ASTM standard G3/89.[32] Such methods, as well as a quantitative analysis (equivalent circuits) in diagrams of the electrochemical impedance spectroscopy technique, were chosen to investigate the tendency of the CR. The EIS tests were conducted using a potentiostat coupled to a frequency analyzer system, a glass corrosion cell kit with a platinum counter electrode, and a saturated calomel reference electrode (SCE). The working electrodes consisted of as-cast Al 9 wt pct Si and Zn 27 wt pct Al alloy samples. These were positioned at the glass corrosion cell kit, leaving a circular 1 cm^2 metal surface in contact with the electrolyte. The potential amplitude was set to 10 mV in open circuit and the frequency range was from 100 mHz to 100 kHz. The samples were further ground up to a 600 grit SiC paper, followed by distilled water washing and air drying before measurements. All of the EIS experiments were duplicated and graphical outputs were obtained.

The polarization tests were conducted by stepping the potential using a scanning rate of 0.2 mV/s from −250 mV (SCE) to +250 mV (SCE) related to open-circuit potential. Using an automatic data acquisition system, the polarization curves were plotted and both corrosion rate and potential were estimated by the Tafel extrapolation method. All the polarization tests were performed after each correspondent EIS test. Thus, both experimental results of electrochemical impedance and polarization tests provided useful information to identify the tendency on the CR. Measurements for EIS tests began after an initial delay of 30 minutes for the sample to reach a steady-state condition. The volume of the electrolyte in the glass corrosion cell kit, for each test, was kept constant. The initial pH values of the electrolyte solution measured before each test were in a range of 6.1 and 6.4.

IV. RESULTS AND DISCUSSION

A. *Solidification Thermal Variables*

The temperature files containing the experimentally monitored temperatures were coupled to a finite difference solidification model for determining the transient metal/mold heat-transfer coefficient (h_i). The method, which is based on the solution of the inverse heat conduction problem, has been used in recent articles to determine h_i for a number of solidification situations.[11–13,21–23,25] Figure 3 shows casting/chill typical experimental thermal responses compared to those numerically simulated and the resulting h_i profiles as a function of time for both Al 9 wt pct Si and Zn 27 wt pct Al alloys.

The results of experimental thermal analysis inside the casting have also been used to determine the tip cooling rate ($\dot{T}_L$), as a function of time or position. The cooling rate was computed by determining the slope of the experimental cooling curves immediately after the passing of the liquidus front by each thermocouple inside the casting.

Figure 4 shows a comparison between the experimental and calculated tip cooling rate as a function of position from the metal/mold interface. The calculated tip cooling rate was obtained by using the analytical expression given by Eq. [3]. In this equation, the appropriate experimental values of h_i, given in Figure 3, and the thermophysical properties, as described in Table II, have been used. A good agreement between experimental results and predictions can be observed. Eventual discrepancies between experimental and calculated tip growth rate are mainly caused by uncertainties in the thermophysical properties and the presence of initial convection currents in the liquid metal induced by fluid motion during pouring, which were not considered by the analytical model.

Figures 5 and 6 exhibit typical Al 9 wt pct Si and Zn 27 wt pct Al microstructures, respectively, observed at longitudinal sections and at different locations from the casting surface.

The main structure of the as-cast hypoeutectic Al-Si alloy (unmodified) consists of an Al-rich dendritic matrix with a eutectic mixture in the interdendritic region formed by needlelike silicon crystals set in an Al-rich phase. The structure of the hypereutectic Zn-Al alloy, immediately after solidification, will be formed by an Al-rich dendritic matrix involved by an interdendritic eutectic mixture.

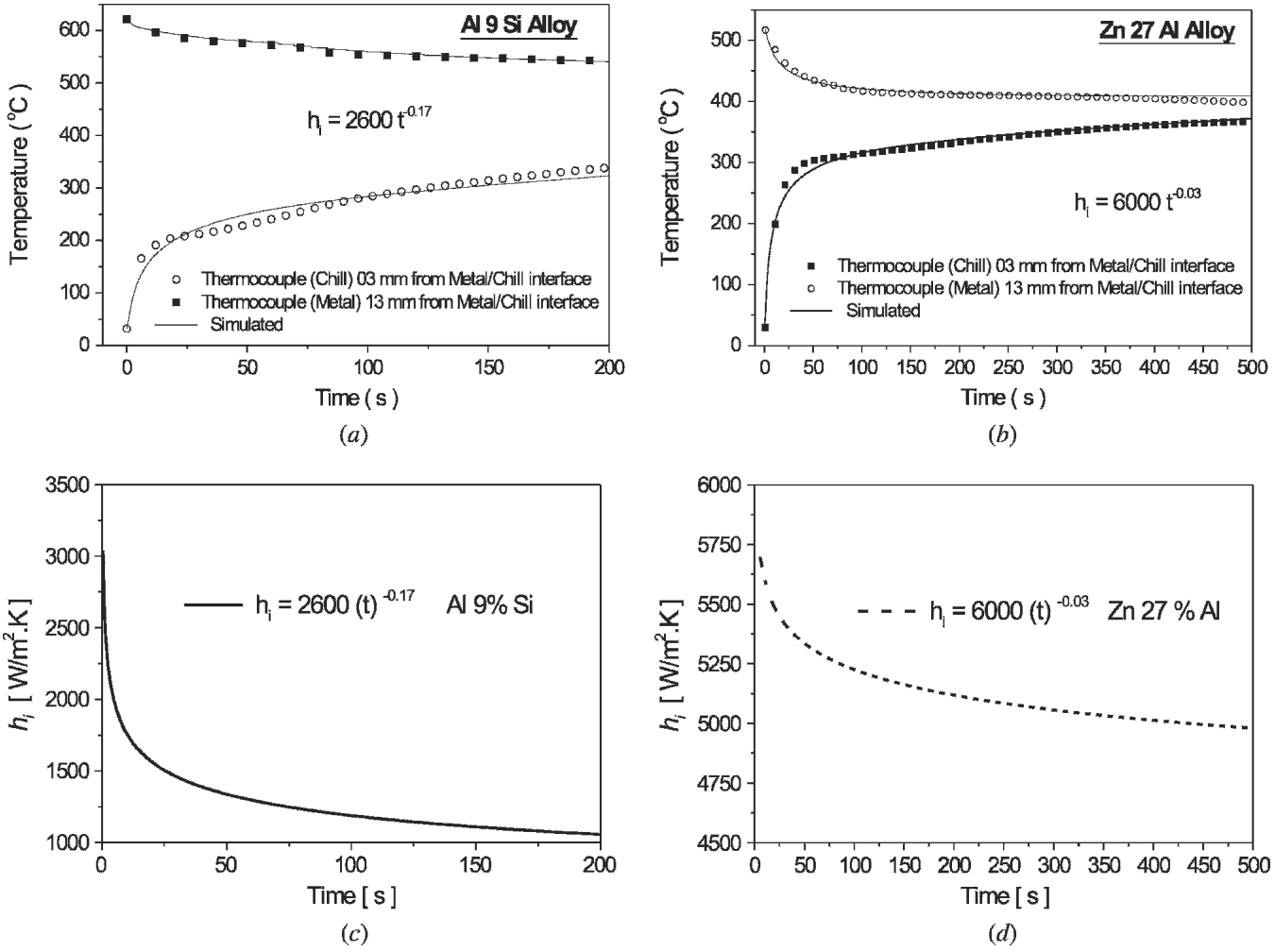

Fig. 3—Typical experimental thermal responses compared to numerical simulations for (*a*) Al 9 wt pct Si and (*b*) Zn 27 wt pct Al alloys and (*c*) and (*d*) the transient metal/mold heat-transfer coefficient h_i (W m^{-2} K^{-1}) as a function of time (s), respectively.

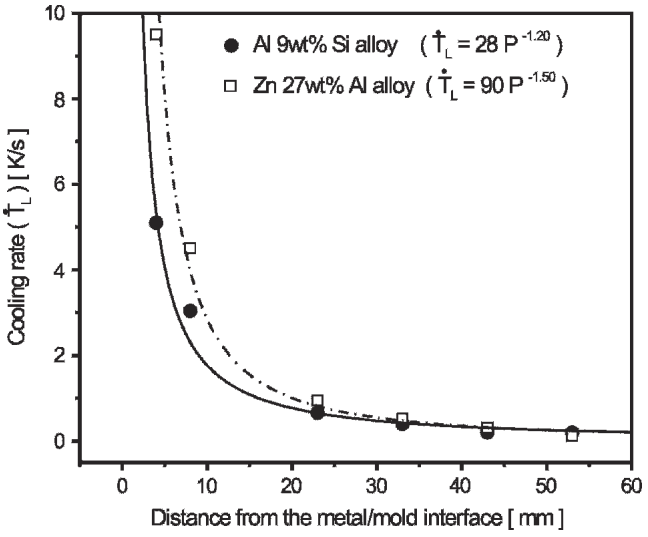

Fig. 4—Comparison between experimental and calculated tip cooling rates Eq. [3] ($\dot{T}_L$), as a function of position from the metal/mold interface for (*a*) Al 9 wt pct Si and (*b*) Zn 27 wt pct Al alloys.

During subsequent cooling, a eutectoid decomposition takes place.[14]

Measurements of secondary dendrite arm spacing (λ_2) as a function of cooling rate ($\dot{T}$) have produced relationships of the form $\lambda_2 \propto \dot{T}^{-b}$, where b is in the range 1/3 to 1/2.[33] Alternatively, this may be given in terms of the local solidification time (t_{SL}), defined as the time taken at a given location inside a casting for the temperature to fall from the liquidus to the nonequilibrium solidus. In such case, $\lambda_2 \propto t_{SL}^b$. Figure 7 shows the measured secondary dendrite arm spacing expressed as a function of distance from the chill/casting interface. It can be observed that, as expected, λ_2 increases due to the decrease in cooling rate with increased distance from the chill/casting surface.

It is important to remark that the secondary spacing is significantly increased due to the contact time between the curved and branched structures and the melt along the solidification range. The ripening process modifies the initial wavelength of secondary arms and can even cause dissolution of tertiary or higher order arms.[34] Several approaches have been proposed to account for the coarsening of dendritic side arms.[35–38] Such approaches may contribute to arm coarsening at different stages of solidification, but they are all driven by the same need to reduce the total surface energy of the system acting through diffusion in the liquid. Kattamis *et al.*[35] have considered that the arms slightly thinner than the average were assumed to laterally melt with transport of material and deposition on larger arms, or alternatively, the arms melt off and material is transported from the roots of the arms to their upper lateral surfaces.

The secondary dendrite arm spacings (λ_2) as a function of tip cooling rate ($\dot{T}_L$) for both Al-9 wt pct Si and Zn 27 wt pct Al alloys are presented in Figure 8. Experimental power laws relating λ_2 with $\dot{T}_L$ were obtained for each case. As expected for both alloys, the secondary arm spacing decreases as the tip growth rate is increased. By comparing the present experimental results for the Al 9 wt pct Si alloy shown in Figure 8 with the general curve of secondary spacings as a function of cooling rate for aluminum alloys, which appears in Prof. Fleming's classic solidification book,[33] a very good agreement can be observed. It can also be seen that a $-1/3$ power law characterizes the experimental scatter. This is in agreement with a report in the literature that shows that, for secondary spacings, an inverse cube root relationship with the cooling rate describes the majority of the metallic binary systems experimentally examined.[39] As can also be seen in Figure 8, for a given cooling rate, the Zn 27 wt pct Al alloy exhibits a coarser dendrite arm spacing when compared with the values corresponding to the Al-Si alloy. The relationship of λ_2 with $\dot{T}_L$ for the Zn-Al alloy is not associated with a $-1/3$ exponent, but rather a $-1/6$ exponent, which fits the experimental scatter. This seems to be associated with the long nonequilibrium freezing range of such alloy ($\Delta T = 108$ °C) and a relatively higher solute diffusivity, which can be conducive to a much more effective coarsening process.

The analytical formula for $\dot{T}_L$, given by Eq. [3], can be inserted into the experimental power laws shown in Figure 8 in order to establish general expressions permitting the secondary dendritic spacing to be expressed as a function of transient solidification variables.

B. *Dendrite Arm Spacing and Mechanical Properties*

Figures 9 and 10 present the experimental results of UTS (σ_U), YS (0.2 pct proof stress) ($\sigma_y = 0.2$), and elongation as a function of secondary dendrite arm spacing (λ_2) for the Al 9 wt pct Si and Zn 27 wt pct Al alloys, respectively. The results are consistent with those found in the literature concerning both Al-Si[1,2] and Zn-Al[5] commercial as-cast alloys. It can be seen for both Al 9 wt pct Si and Zn 27 wt pct Al alloys that UTS and elongation increase with decreasing secondary spacing.

The improvement of strength by a reduction in λ_2 seems to be the result of the number of separate effects, all of which seem to operate beneficially. Slight faults during growth will cause the dendrite arms within a grain to become slightly misoriented, and the higher the degree of misorientation, the greater the resistance will be to the passage of a slip plane. Other contributions to the difficulty of propagating slip across the interdendritic region include the presence of segregated solute, which would alter the local hardness by solute strengthening, and possibly by precipitation of other phases. Also, there may be present macroscopic particles that may be hard and strong, so constituting effective barriers to slip. As λ_2 is reduced, the cast structure becomes cleaner and sounder, and these qualities are important contributors to improved properties.[40]

For both cases experimentally examined in the current study, a more homogeneous distribution of the eutectic mixture for smaller spacings seems to contribute to the increase in UTS. However, the increase in solidification rate has other general beneficial attributes, such as reduction in gas porosity (in the present experiments, the alloys were degassed just before pouring), more refined eutectic structure (finer silicon crystals for the Al-Si alloy), and greater solute saturation. Therefore, the observed improvement in tensile properties cannot be attributed solely to smaller dendritic spacings.

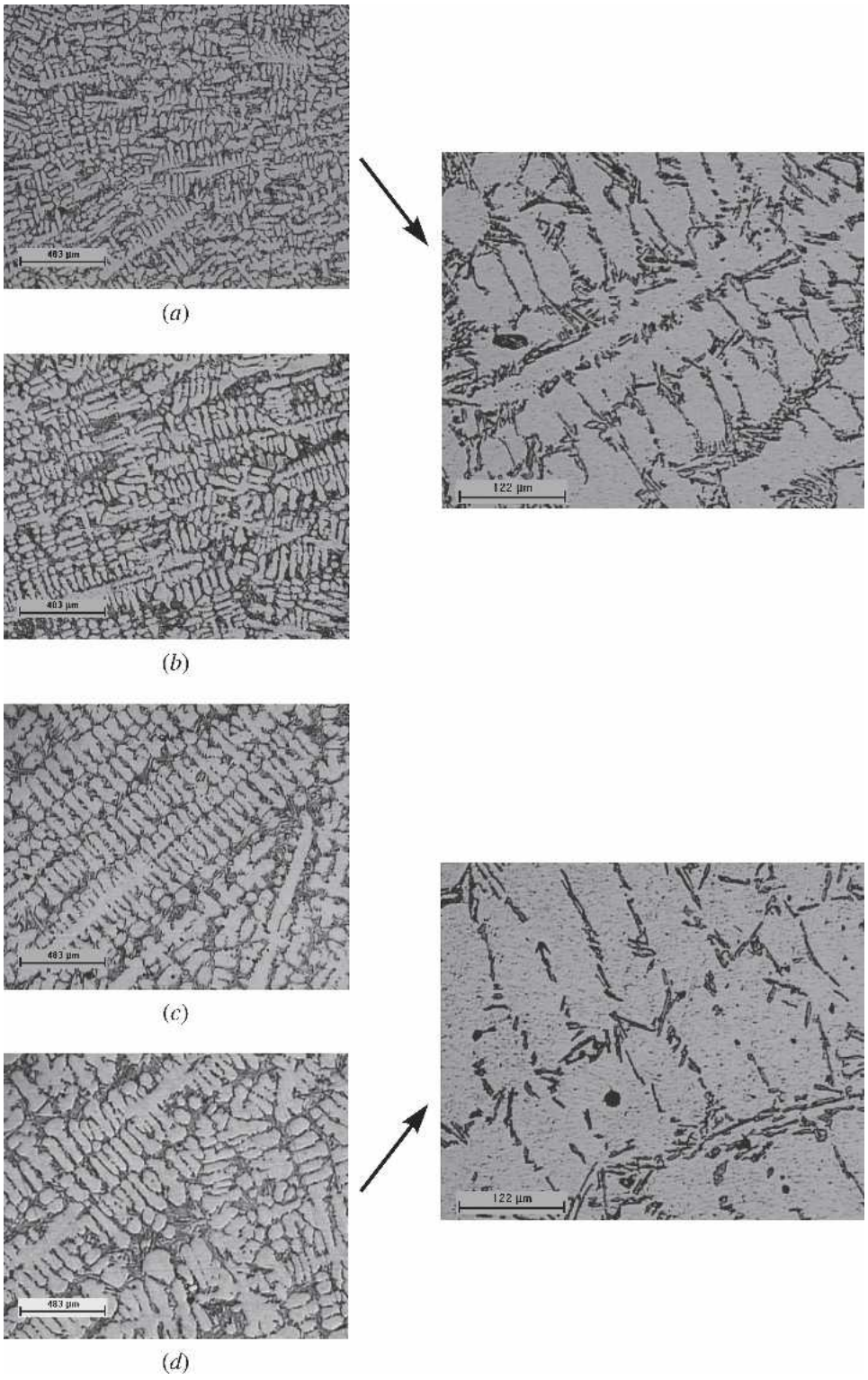

Fig. 5—Typical microstructures of longitudinal sections of Al 9 wt pct Si alloy samples at (*a*) 10 mm, (*b*) 20 mm, (*c*) 40 mm, and (*d*) 60 mm from the chill/casting interface.

It can also be observed in Figures 9 and 10 that the YS is essentially constant with increasing secondary dendrite arm spacing for the Al-Si alloy, but increases significantly with decreasing λ_2 for the Zn-Al alloy. A similar observation concerning a commercial Al 7 wt pct Si alloy has also been reported in the literature.[2] It should be emphasized that the 0.2 pct proof stress does not strictly represent the limit between elastic and plastic tensile properties. The dendritic spacing is not expected to affect significantly the elastic deformation, but it will affect the plastic deformation so

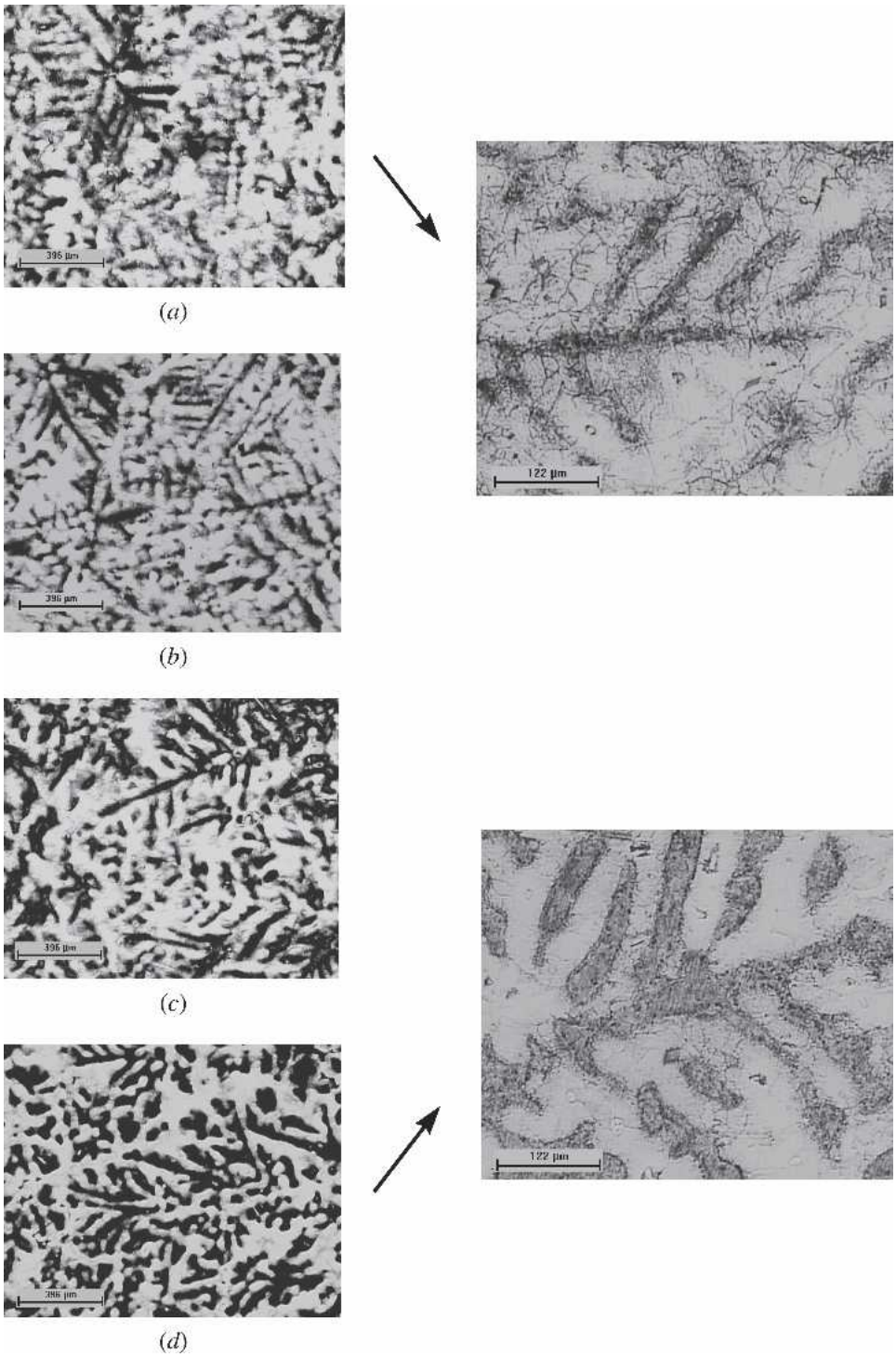

Fig. 6—Typical microstructures of longitudinal sections of Zn 27 wt pct Al alloy samples at (*a*) 10 mm, (*b*) 20 mm, (*c*) 40 mm, and (*d*) 60 mm from the chill/casting interface.

that the influence will depend on how deep in the plastic region the proof stress will be located and on the particular progress of plastic deformation of each alloy. The different behavior on YS with λ_2 seems to be associated with such factors. The deformation of the Zn-Al alloy is typical of alloys formed by two different metallic solid solutions, while the deformation in the Al-Si alloy proceeds by slip in the Al-rich matrix accomodated by a progressive fracture in the increasing number of silicon particles.

The experimental equations appearing in Figures 9 and 10 can incorporate models expressing λ_2 as a function of thermal solidification variables (including metal/mold heat-transfer coefficient), such as Eq. [3], permitting expressions correlating mechanical properties with solidification conditions

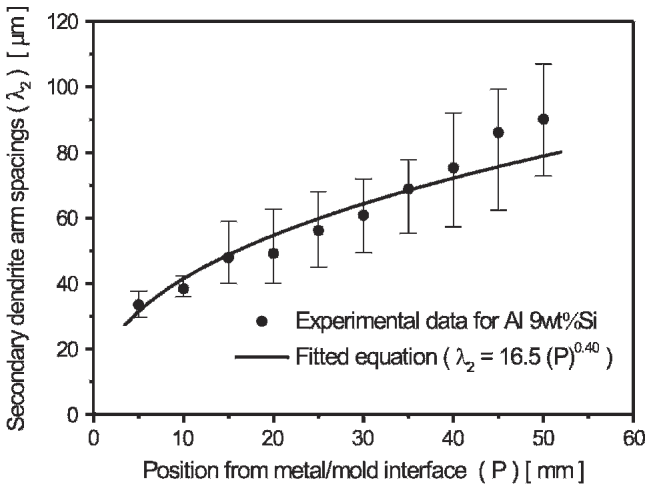

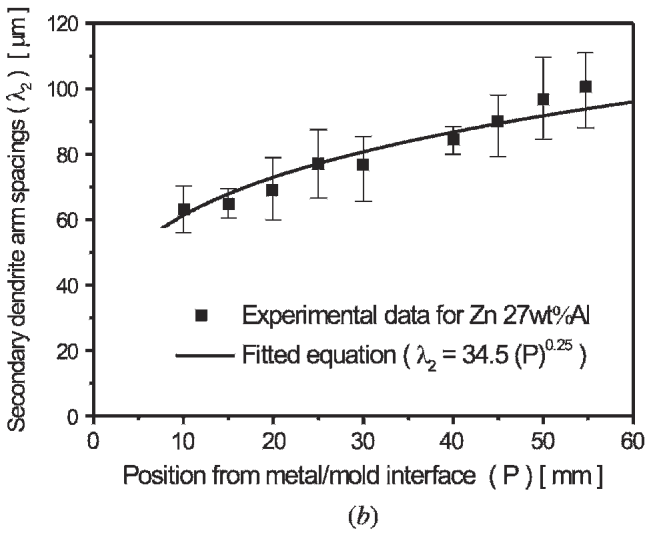

Fig. 7—Secondary dendrite arm spacing (λ_2) as a function of position from the chill/casting interface for (*a*) Al 9 wt pct Si and (*b*) Zn 27 wt pct Al alloys.

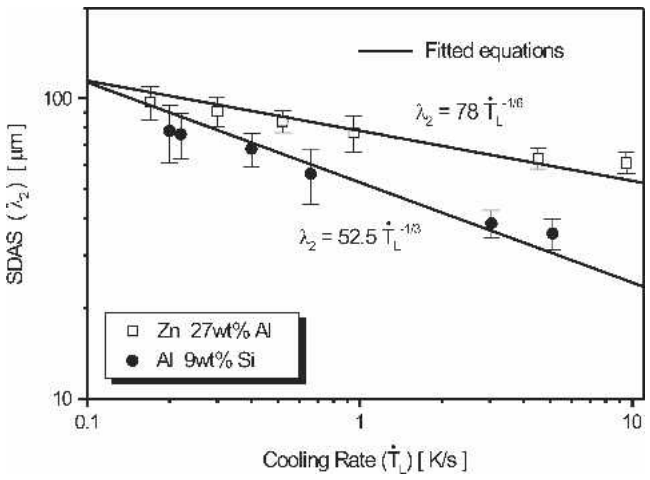

Fig. 8—Experimental secondary dendrite arm spacing (λ_2) *vs* tip cooling rate ($\dot{T}_L$) for Al 9 wt pct Si and Zn 27 wt pct Al alloys.

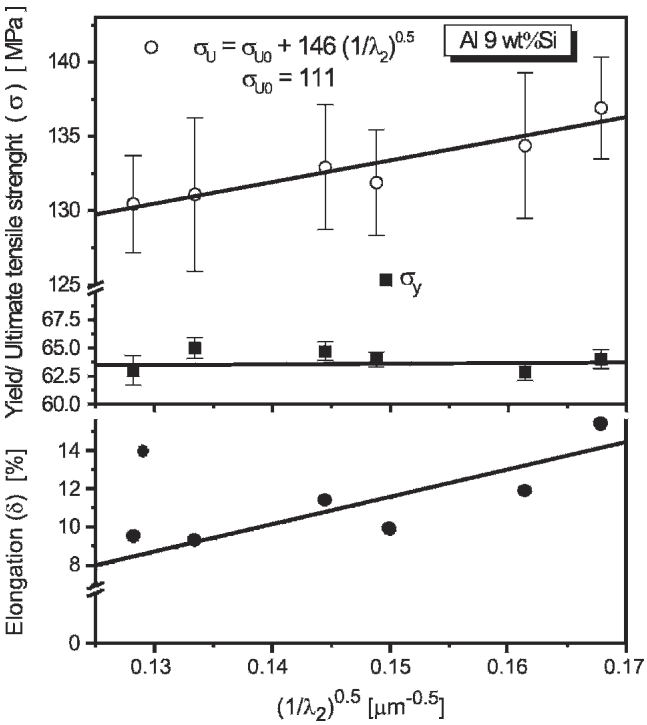

Fig. 9—UTS (σ_u), YS (0.2 pct proof stress) ($\sigma_y = 0.2$), and elongation as a function of secondary dendrite arm spacing (λ_2) for an Al 9 wt pct Si alloy casting.

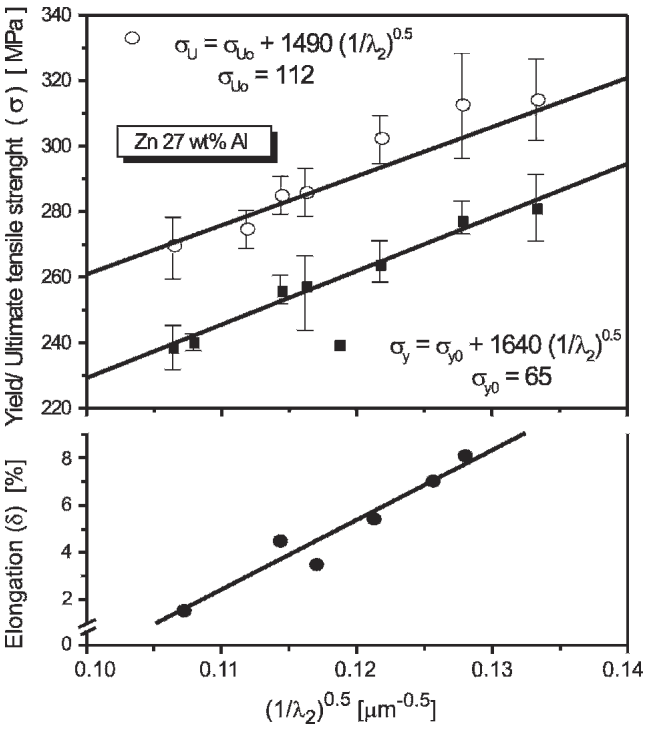

Fig. 10—UTS (σ_u), YS (0.2 pct proof stress) ($\sigma_y = 0.2$), and elongation as a function of secondary dendrite arm spacing (λ_2) for an Zn 27 wt pct Al alloy casting.

to be established. Previous articles have established general expressions correlating mechanical properties, solidification thermal variables, and the resultant microstructure

for hypoeutectic Al-Cu[13] and hypoeutectic Zn-Al alloys.[11]

C. *Dendrite Arm Spacing and Corrosion Behavior*

In order to investigate the CR tendency on both Al-9Si and Zn-27Al alloys as a function of secondary dendrite arm spacing, a number of samples collected along the ingot length, as shown in Figure 11, were subjected to corrosion tests (EIS and Tafel polarization techniques).

Each position exhibits a different mean secondary dendrite arm spacing, as shown in Figure 7, which is directly associated with the local cooling rate during solidification.

Figure 12 shows a comparison of experimental results concerning EIS diagrams and potentiodynamic polarization curves at four and five different positions from the chill/casting surfaces for Al 9 wt pct Si and Zn 27 wt pct Al alloys, respectively. The equivalent circuit and impedance parameters are shown in Figure 13 and Table III, respectively. Qualitative and quantitative analysis from the EIS diagrams, *i.e.*, impedance parameters (polarization resistance and capacitances values),[41,42] current density, and corrosion potential (obtained from potentiodynamic polarization curves) permit observation of a similar tendency of CR for Al 9 wt pct Si and Zn 27 wt pct Al alloys. It is observed that the CR increases with distance from the chill/casting interface.

As a direct consequence, the modulus of impedance (polarization resistance, R_1) and the phase angle increase with increasing secondary dendrite arm spacing. It is well known that higher impedance and phase angle are conducive to nobler electrochemical behavior.

Analysis of EIS diagrams for both Al 9 wt pct Si and Zn 27 wt pct Al alloys (Figure 12) and impedance parameters such as polarization resistance (R_1) and capacitances values (Z_{CPE}),[41,42] indicated in Table III (each value represents an average of three tests), permit the conclusion that the tendency of CR increases with increasing distance (position) from the chill/casting surface. As a direct consequence, CR increases with increasing secondary dendrite arm spacing.

It can be seen in Table III that, at position P1 (λ_2 = 35 to 40 μm), the capacitance of the Al 9 wt pct Si sample is of about 70 $10^6/\Omega^{-1}$ s^n cm^{-2} (or 70 μFcm^{-2}) and the polarization resistance 2385 Ωcm^{-2}. On the other hand, at position P4 (coarser structure), the Al 9 wt pct Si sample presents a lower capacitance and a higher polarization resistance than those of position P1, as indicated in Table III. The increase in R1 associated with a decrease in capacitance is conducive to improvements in CR. The CR tendency can be better observed when analyzing the potentiodynamic polarization curves. For example, current density (corrosion rate) at P1 is higher than those at subsequent positions, as shown in Figures 12(c) and (f). The Al 9 wt pct Si alloy presents the following sequence of corrosion rates

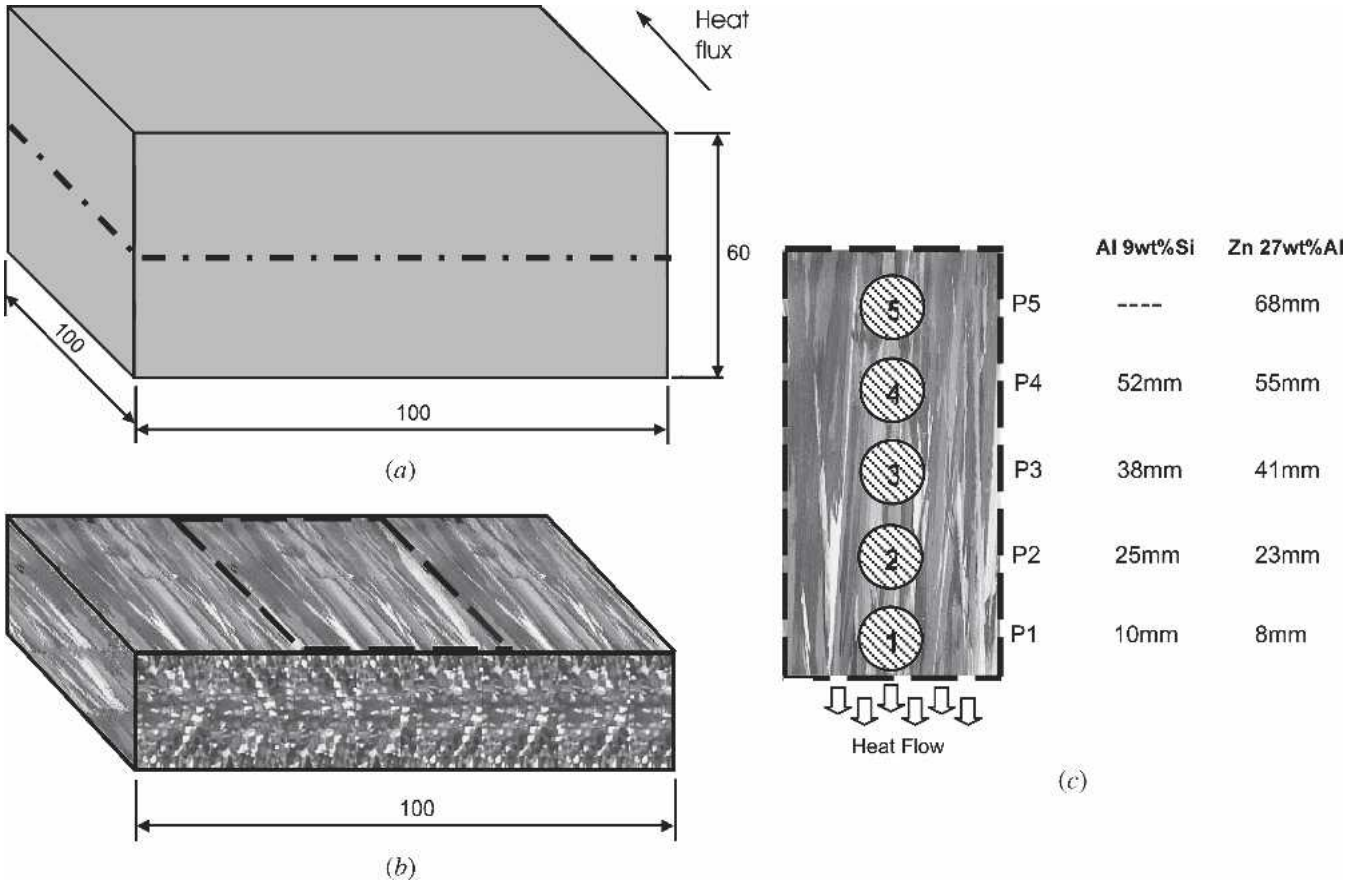

Fig. 11—Schematic representation: (*a*) ingot, (*b*) macroetched half-ingot, and (*c*) selected distances from the casting surface for corrosion tests for both Al 9 wt pct Si and Zn 27 wt pct Al alloys.

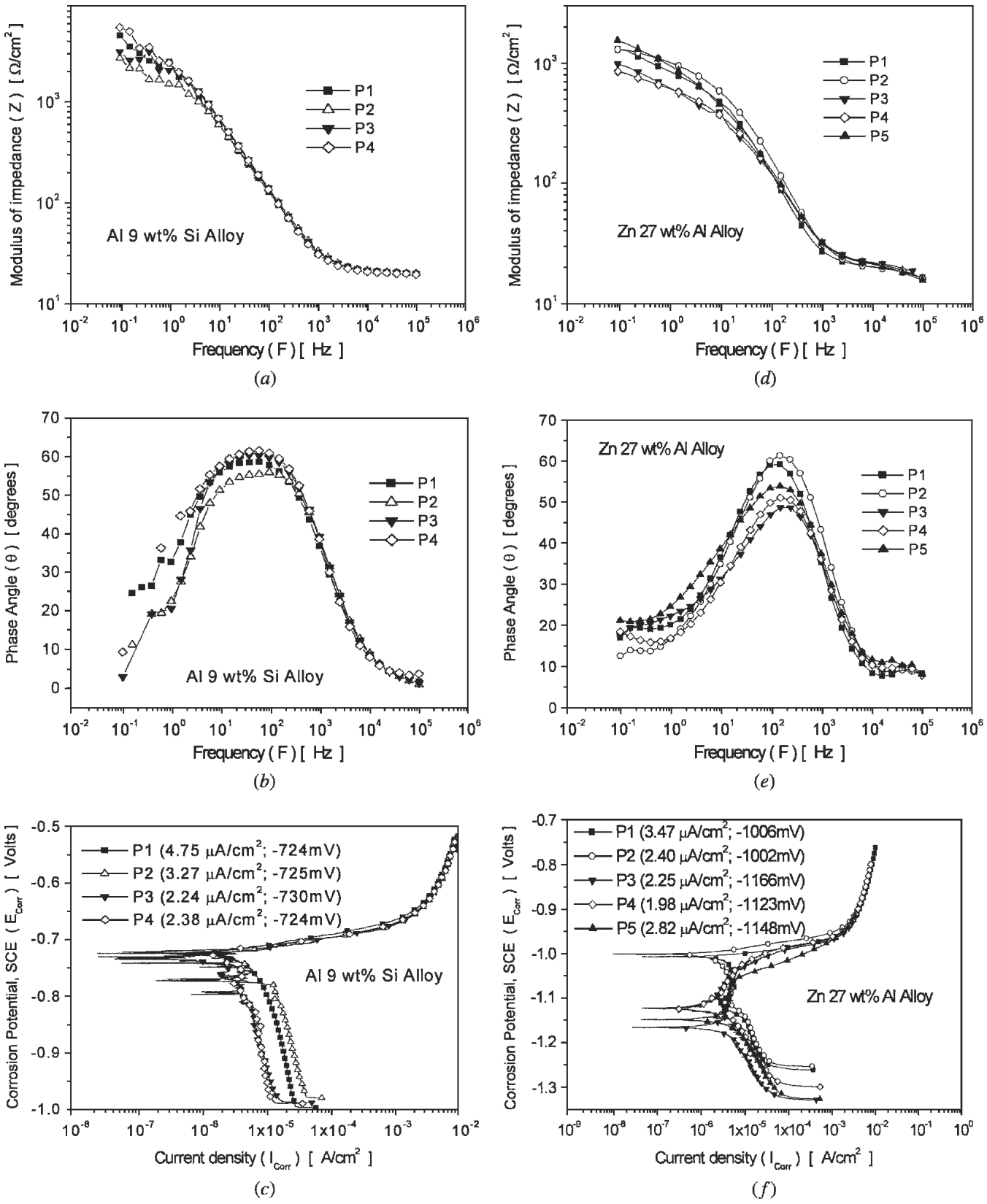

Fig. 12—EIS diagrams (Bode and Bode phase) and potentiodynamic polarization curves at different positions from the metal/mold interface for (*a*) through (*c*) Al 9 wt pct Si and (*d*) through (*f*) Zn 27 wt pct Al alloys.

as a function of the distance from the casting/chill interface P1 (4.75 μA/cm^2), P2 (3.27 μA/cm^2), P3 (2.24 μA/cm^2), and P4 (2.38 μA/cm^2). The Zn-27Al alloy shows the following sequence P1 (3.47 μA/cm^2), P2 (2.40 μA/cm^2), P3 (2.25 μA/cm^2), P4 (1.98 μA/cm^2), and P5 (2.82 μA/cm^2). Thus, it can be seen that both Al 9 wt pct Si and Zn 27 wt pct Al alloys show current density decreasing as the secondary dendrite arm spacing is increased, as indicated in Figures 12(c) and (f).

It is also important to remark that P3 and P4 for the Al 9 wt pct Si alloy are positions located on both sides of the CET transition, respectively, and present similar corrosion rates. In a recent study,[14] similar effects of CET structures upon the CR of binary alloys have been reported.

Analysis of experimental and calculated EIS results (Table III) and potentiodynamic polarization curves (Figures 12(c) and (f)) permits to confirm that coarser dendritic structures tend to improve the CR of both Al 9 wt pct Si and Zn 27 wt pct Al alloys.

For the Al 9 wt pct Si alloy, the Al-rich dendritic matrix is delimited by interdendritic regions that are also constituted by a eutectic mixture, *i.e.*, Al-rich phase and Si particles, as shown in Figure 14. However, the eutectic morphology is not lamellar but, rather, is formed by Si particles disseminated throughout the Al-rich phase. From the electrochemical point of view, Si is nobler than Al, so that the latter will be more susceptible to corrosion when immersed in some aggressive environment. However, the Al-rich (α) phase and Si have dissimilar growth behaviors with Si growing from the liquid in a faceted manner (smooth growth interface) while the α phase solidifies with surfaces that are rough. The interdendritic regions will be constituted by both phases and special attention should be given to the boundary between these phases (Figure 14(b)).

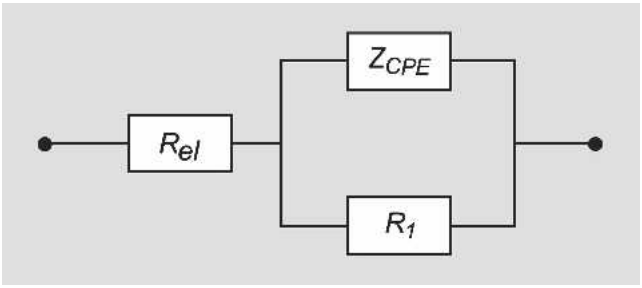

Fig. 13—Equivalent circuit for modeling impedance data of the examined alloys.

Because of the different mentioned growth mechanisms of each phase, their boundaries will not be perfectly conformed, but rather will be subjected to a certain deformation in the atomic level, mainly on the α phase side of the interface. It seems that these regions, because of such localized deformation, could be more susceptible to corrosion than α phase regions, which are not so close to the Si particles. This could explain the present experimental results; *i.e.*, a coarser dendritic structure would exhibit a higher tendency of improvement in the CR for the Al-Si alloy since smaller dendritic spacings result equally in smaller interdendritic areas and in more extensive distribution of silicon particles throughout the casting (thus contributing to dissemination of areas where corrosion could be initiated and develop).

For the Zn 27 wt pct Al alloy, it is known that the final microstructure at room temperature will be composed of an Al-rich dendritic matrix and an interdendritic lamellar eutectic mixture. The morphology of the eutectoid transformation seems to not be affected. The corrosion performance of hypereutectic Zn-Al alloys will be more affected by the contiguous nonlamellar deposition of the two phases, which occurs during eutectoid decomposition of such Zn-Al alloys, and coarser dendritic structures will tend to improve their CR.[14]

D. *Correlation between CR and Mechanical Properties*

Figure 15 shows curves of corrosion rate tendency for both Al 9 wt pct Si and Zn 27 wt pct Al alloys as a function of position from the casting/chill interface. It can be observed that these two alloys present a similar corrosion rate (of about 2.4 μA/cm^2) at position 3 (of about 35 and 40 mm from the metal/mold interface). At this position, the

Table III. Impedance Parameters for Samples of Al 9 Wt Pct Si and Zn 27 Wt Pct Al Alloys in 3 Pct NaCl Solution

	Al 9 Wt Pct Si Alloy			
Parameters	P1* (35 to 40 μm)	P2 (55 to 62 μm)	P3 (68 to 75 μm)	P4 (80 to 85 μm)
R_{el} (Ω cm^{-2})	18.5	18.7	19	18
Z_{CPE} ($10^6/\Omega^{-1}$ s^n cm^{-2})	$70.15^{\pm 4.2}$	$66.95^{\pm 4.6}$	$54.11^{\pm 3.7}$	$52.13^{\pm 2.2}$
n	0.72	0.72	0.77	0.77
R_1 (Ω cm^{-2})	2385	3858	4069	5367

	Zn 27 Wt Pct Al Alloy				
Parameters	P1 (55 to 62 μm)	P2 (70 to 75 μm)	P3 (85 to 90 μm)	P4 (92 to 95 μm)	P5 (95 to 100 μm)
R_{el} (Ω cm^{-2})	17	17	16	17	16
Z_{CPE} ($10^6/\Omega^{-1}$ s^n cm^{-2})	$58.08^{\pm 3.2}$	$44.81^{\pm 2.6}$	$61.77^{\pm 4.7}$	$55.88^{\pm 3.4}$	$70.85^{\pm 4.6}$
n	0.76	0.77	0.72	0.74	0.72
R_1 (Ω cm^{-2})	1083	1165	720	660	1289

*P1 through P4 or P5 represent the different positions (distance) from the metal/mold interface, as shown in Fig. 11(c).

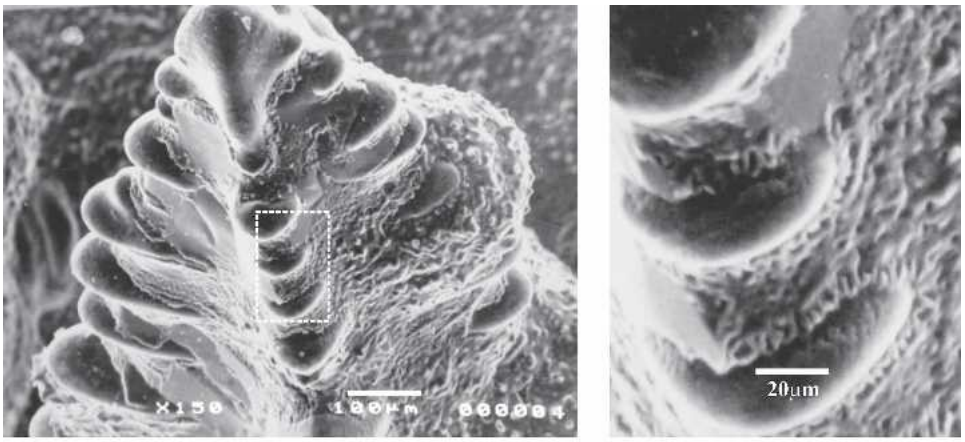

Fig. 14—Typical SEM dendritic microstructure of an Al-Si hypoeutectic alloy: (*a*) dendritic matrix and (*b*) detail of secondary arm spacing and interdendritic region.

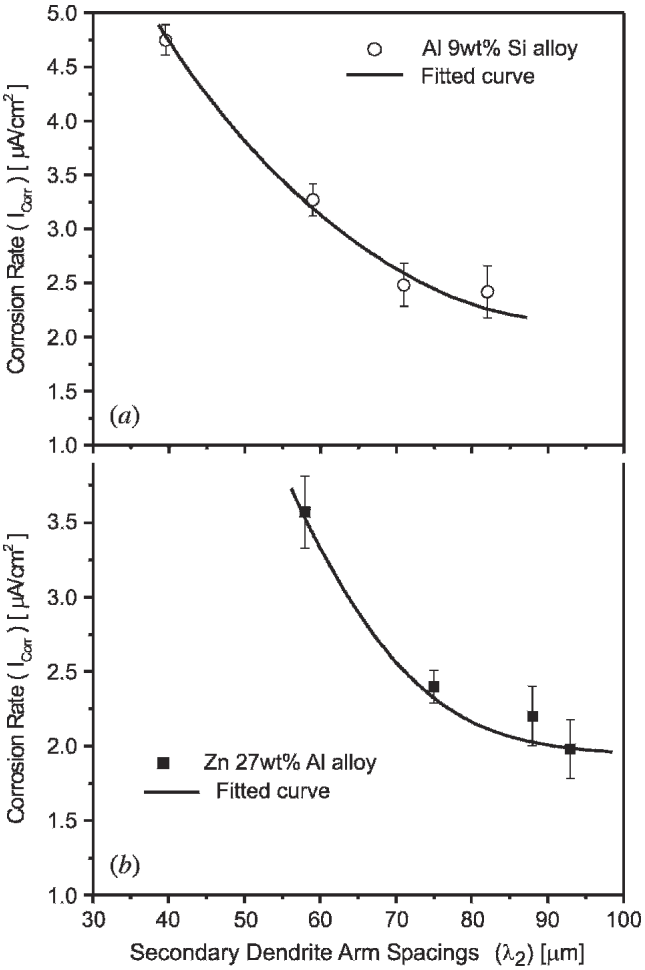

Fig. 15—Corrosion rate tendency as a function of position from casting surface for (*a*) Al 9 wt pct Si and (*b*) Zn 27 wt pct Al alloys.

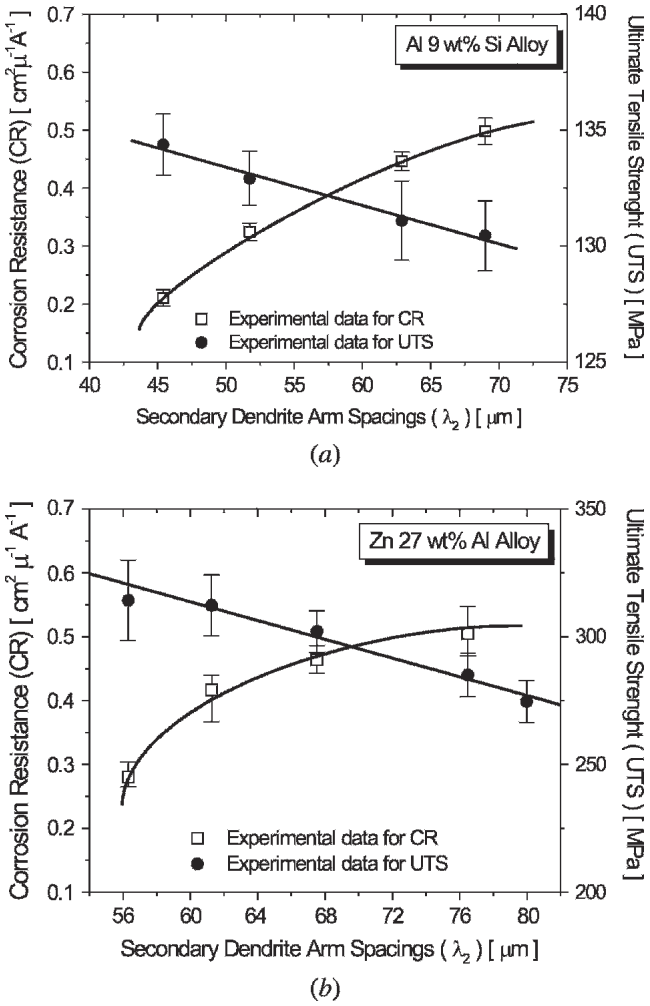

Fig. 16—CR and UTS as a function of secondary dendrite spacing (λ_2) for (*a*) as-cast Al 9 wt pct Si and (*b*) Zn 27 wt pct Al alloys.

secondary dendrite arm spacings are about 70 and 90 μm for Al 9 wt pct Si and Zn 27 wt pct Al alloys, respectively.

Figure 16 combines CR and UTS plotted as a function of secondary dendrite arm spacing for both Al 9 wt pct Si and Zn 27 wt pct Al alloys. In order to compare the behavior of CR and tensile strength, the CR is represented by the inverse of the corrosion rate, as shown in Figure 15. The

UTS values are those indicated in Figures 9 and 10 for Al 9 wt pct Si and Zn 27 wt pct Al alloys, respectively. It is well known that the great challenge in engineering applications is the improvement of a property without provoking deleterious effects in another property. Thus, the aim of such combined plots is to design an ''ideal'' range of microstructural dendritic spacings, which determines a region with a compromise between good CR and good UTS for these alloys. Evidently, for some specific application where one such characteristic should be more significant than the other one, this range of equilibrium between CR and UTS should not be considered.

V. CONCLUSIONS

The following main conclusions can be drawn from the present experimental investigation.

1. For both Al 9 wt pct Si and Zn 27 wt pct Al alloys, the UTS and elongation increase with decreasing secondary dendrite arm spacing (λ_2). In both cases, a more homogeneous distribution of the eutectic mixture for smaller spacings seems to be responsible for the increase in tensile strength. The resulting experimental equations of UTS and YS as a function of λ_2 can be connected with models expressing λ_2 as a function of solidification thermal variables (including transient metal/mold heat-transfer coefficient) permitting expressions correlating mechanical properties with solidification conditions to be established.
2. The experimental EIS diagrams, potentiodynamic curves, and fitted equivalent circuit parameters have shown that coarser dendritic structures tend to yield higher CR than finer dendritic structures for both Al 9 wt pct Si and Zn 27 wt pct Al alloys. For the former alloy, such tendency of better CR presented by coarser dendritic microstructures seems to be associated with the growth morphology of the two phases that constitute the interdendritic eutectic mixture. For the Zn 27 wt pct Al alloy, the better CR tendency for coarser dendrite arms is connected with the final microstructure, resulting from the contiguous nonlamellar deposition of the two phases, which occurs during the eutectoid decomposition.
3. The control of as-cast microstructures, by manipulating solidification processing variables, permitting the control of cooling rate and tip growth rate, can be used as an alternative way to produce components with a compromise between good corrosion behavior and good mechanical properties, which occurs for a specific range of dendritic arm spacings.

ACKNOWLEDGMENTS

The authors acknowledge the financial support provided by FAEP-UNICAMP, FAPESP (The Scientific Research Foundation of the State of São Paulo, Brazil), and CNPq (The Brazilian Research Council).

REFERENCES

1. S.G. Shabestari and H. Moemeni: *J. Mater. Proc. Technol.*, 2004, vol. 153 (4), pp. 193-98.
2. E.L. Rooy: *Metals Handbook*, vol. 15, *Castings*, ASM INTERNATIONAL, Metals Park, OH, 1988, vol. 15, pp. 743-70.
3. J. Birch: *Mater. Des.*, 1990, vol. 11, pp. 83-87.
4. Ç. Fatih and S. Kurnaz: *Mater. Des.*, 2005, vol. 25, pp. 479-85.
5. M. Durman: *Z. Metallkd.*, 1998, vol. 89, pp. 417-23.
6. N.J. Petch: *J. Iron Steel Inst.*, 1953, vol. 174, pp. 25-31.
7. A. Lasalmonie and J. Strudel: *J. Mater. Sci.*, 1986, vol. 21, pp. 1837-52.
8. K.J. Kurzydlowski, B. Ralph, J.J. Bucki, and A. Garbacz: *Mater. Sci. Eng., A*, 1996, vol. 205, pp. 127-32.
9. D. Dubé, A. Couture, Y. Carbonneaut, M. Fiset, R. Angers, and R. Tremblay: *Int. J. Cast Met. Res.*, 1998, vol. 11, pp. 139-44.
10. P. Donelan: *Mater. Sci. Technol.*, 2000, vol. 16, pp. 261-69.
11. W.R. Osório and A. Garcia: *Mater. Sci. Eng. A*, 2002, vol. 325, pp. 103-11.
12. W.R. Osório, C.A. Santos, J.M.V. Quaresma, and A. Garcia: *J. Mater. Proc. Technol.*, 2003, vol. 143, pp. 703-09.
13. J.M. Quaresma, C.A. Santos, and A. Garcia: *Metall. Mater. Trans. A*, 2000, vol. 31A, pp. 3167-78.
14. W.R. Osório, C.M.A. Freire, and A. Garcia: *J. Alloys Compounds*, 2005, vol. 397, pp. 179-91.
15. W.R. Osório, J.E. Spinelli, N. Cheung, and A. Garcia: *Mater. Sci. Eng., A*, 2006, vol. 420, pp. 179-86.
16. W.R. Osório, C.M.A. Freire, and A. Garcia: *J. Mater. Sci.*, 2005, vol. 40, pp. 4493-99.
17. G. Song, A. Atrens, and M. Dareusch: *Corr. Sci.*, 1999, vol. 41, pp. 249-73.
18. G. Song, A.L. Bowles, and D.H. St. John: *Mater. Sci. Eng., A*, 2004, vol. 366, pp. 74-86.
19. B. Yu and J. Uan: *Metall. Mater. Trans. A*, 2005, vol. 36A, pp. 2245-52.
20. W.R. Osório, C.M.A. Freire, and A. Garcia: *Mater. Sci. Eng., A*, 2005, vol. 402, pp. 22-32.
21. W.R. Osório, C.M.A. Freire, and A. Garcia: *Rev. Met. Madrid*, 2005, vol. Extr., pp. 176-80.
22. C.A. Siqueira, N. Cheung, and A. Garcia: *Metall. Mater. Trans. A*, 2002, vol. 33A, pp. 2107-18.
23. O.L. Rocha, C.A. Siqueira, and A. Garcia: *Metall. Mater. Trans. A*, 2003, vol. 34A, pp. 995-1006.
24. A. Garcia, T.W. Clyne, and M. Prates: *Metall. Trans. B*, 1979, vol. 10B, pp. 85-9.
25. I.L. Ferreira, C.A. Santos, V.R. Voller, and A. Garcia: *Metall. Mater. Trans. B*, 2004, vol. 35B, pp. 285-97.
26. F. Sá, O.L. Rocha, C.A. Siqueira, and A. Garcia: *Mater. Sci. Eng., A*, 2004, vol. 373, pp. 131-38.
27. M.D. Peres, C.A. Siqueira, and A. Garcia: *J. Alloys Compounds*, 2004, vol. 381, pp. 168-81.
28. J.E. Spinelli, M.D. Peres, and A. Garcia: *J. Alloys Compounds*, 2005, vol. 403, pp. 228-38.
29. N. Tunca and R.W. Smith: *J. Mater. Sci.*, 1988, vol. 23, pp. 111-20.
30. C.A. Gandin: *Acta Mater.*, 2000, vol. 48, pp. 2483-501.
31. C.A. Siqueira, N. Cheung, and A. Garcia: *J. Alloys Compounds*, 2003, vol. 351, pp. 126-34.
32. *Standard Recommended Practice for Conventions Applicable to Electrochemical Measurements in Corrosion Tests*, ASTM G3, ASTM, Philadelphia, PA, 1989.
33. M.C. Flemings: *Solidification Processing*, McGraw Hill, Inc., New York, NY, 1974, pp. 148-50.
34. W. Kurz and D.J. Fisher: *Fundamentals of Solidification*, Trans Tech Publications Ltd., Aedermannsdorf, Switzerland, 1986, pp. 73-77.
35. T.Z. Kattamis, J.C. Coughlin, and M.C. Flemings: *Trans. TMS-AIME*, 1967, vol. 239, pp. 1504-11.
36. M. Chen and T.Z. Kattamis: *Mater. Sci. Eng., A*, 1998, vol. 247, pp. 239-47.
37. D.H. Kirkwood: *Mater. Sci. Eng., A*, 1985, vol. 73, pp. L1-L4.
38. A. Mortensen: *Metall. Mater. Trans. B*, 1996, vol. 27B, pp. 101-13.
39. D. Bouchard and J.S. Kirkaldy: *Metall. Mater. Trans. B*, 1997, vol. 28B, pp. 651-63.
40. J. Campbell: *Castings*, Butterworth-Heinemann, Oxford, United Kingdom, 1991, pp. 264-67.
41. M. Kliskic, J. Radosevic, S. Gudic, and M. Smith: *Electrochem. Acta*, 1998, vol. 43, pp. 3241-55.
42. S. Gudic, J. Radosevic, and M. Kliskic: *Electrochem. Acta.*, 2002, vol. 47, pp. 3009-16.